JREE: Vol. 5, No. 4, (Fall 2018) 18-26

Journal of Renewable Energy and Environment

Research Article

Journal Homepage: www.jree.ir

A New Sensitivity Study of Thermal Stress Distribution for a Planar Solid Oxide Fuel Cell

Imad-Eddine Fahs*, Majid Ghassemi

Mechanical Engineering Faculty, K.N. Toosi University of Technology, Tehran, Iran.

PAPER INFO

Paper history:
Received 07 June 2019
Accepted in revised form 07 October 2019

Keywords:
Solid Oxide Fuel Cell
Computational Fluid Dynamic
Finite Elements
Thermal Stress
Stress Intensity Factor
Crack Initiation

ABSTRACT

Converting chemical energy into electricity is done by an electro-chemical device known as a fuel cell. Thermal stress is caused at high operating temperature between 700 °C to 1000 °C of SOFC. Thermal stress causes gas escape, structure variability, crack initiation, crack propagation, and cease operation of the SOFC before its lifetime. The aim of this study is to present a method that predicts the initiation of cracks in an anisotropic porous planar SOFC. The temperature and stress distribution are calculated. The code uses the generated data, stress intensity factor, and the J-integral of the materials to predict the initiation of the crack inside the porous anode and cathode. The results show that the highest thermal stress occurs at the upper corners of cathode and at the lower corners of the anode. In addition, the thickness of cathode electrode on the left side is increased by 1.5 %. Finally, the crack initiation occurs on the left side between the upper and lower corners of the cathode.

1. INTRODUCTION

One of the greatest and promising new energy technologies for high energy efficiency is a fuel cell, which is also environmental responsive and shows fuel variety [1]. Fuel cells are electrochemical mechanisms that transform chemical energy into electrical and thermal energy. SOFCs, one of the different types of fuel cells, have received much attention due to their high performance and fuel flexibility [2,3]. In addition to that, they function in the high-temperature variety ranging between 700 °C–1000 °C. However, this technology still faces many challenges such as cost reduction and an extended lifetime operation. These challenges require prediction and prevention of internal thermal stresses. The number of SOFC experimental and numerical research papers has shown a prosperous increase throughout the last 20 years [4-10]. While experimental studies focus on the performance of the fuels and materials, numerical studies take into account the embedded physical, chemical, and electro-chemical incidents that take place inside the cell. (Pasaogullari and Wang) [11]. Several researchers used 3D for modeling the entire fuel cell [12,13]. The common objective of their research was to study different configurations and many operating conditions and their effect on the overall cell performance. On the other hand, other researchers tended to use models of two dimensions (2D) to simulate tubular SOFCs for their axial [14]. Another class of studies analyzes the phenomena that occur close to the porous electrodes and electrolyte. Recently, most researchers have focused on the thermal stress inside the SOFC and studied stress in 2D model and the thermal analysis in the anode-electrolyte boundary of SOFC.

Pianko et al. studied the modeling of thermal stresses in a micro tubular Solid Oxide Fuel Cell stack. They presented a detailed mechanical analysis of a new design of the micro tubular Solid Oxide Fuel Cell stack supported fuel cells distributed over the circumference in four rows. In this paper, they analyzed the residual stresses induced in the anode-electrolyte-cathode assembly of the sintered fuel cell layers and analyzed the effect of spatial temperature gradient on the stress distribution in the SOFC stack. Furthermore, the influence of temperature non-uniformity among fuel cells and the SOFC stack with supporting structure on stress distributions was studied. The numerical results used to determine the areas of high stress values were higher than the yield strength of materials. Further, they analyzed the degradation of anode-supported intermediate temperature-solid oxide fuel cells under various failure modes. Their model solved the fluid flow, heat, and mass transfer separately. However, it did not cover thermal degradation and crack initiation [15]. Pianko et al. studied the modeling of thermal stresses in a planar Solid Oxide Fuel Cell and made a comparison of thermal stress distribution at different voltages (0.3, 0.7, and 1.1 v). However, Pianko study did not cover thermal degradation and pressure distribution in the whole cell. In addition, they did not take into consideration the mechanical equations and mechanical properties [16].

The purpose of the current paper is to present a method that predicts the initiation of cracks in an anisotropic porous planar SOFC. The main goal is to understand the effect of thermal stress and high temperature on crack initiation and its location for future remedy.

2. PROBLEM DEFINISION

The diagram of the problem is represented in Fig.1. As shown in Fig. 1, the cell consists of 5 layers, anode, cathode, electrolyte, air channel, and fuel channel. Tables 1 and 2 show the material properties and the geometrical parameters of the current study, respectively.

*Corresponding Author's Email: imadfahs@email.kntu.ac.ir (I. Fahs)

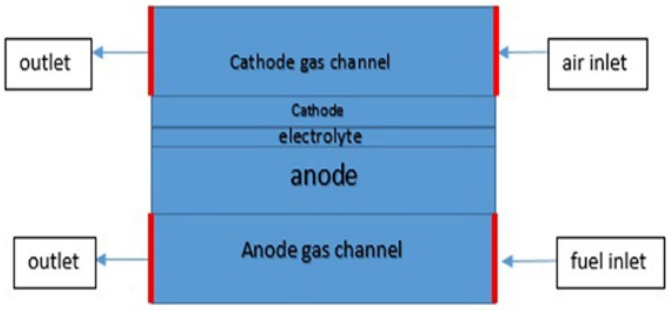

Figure 1. solid oxide fuel cell [17].

Table 1. Material properties of the SOFC.

	Anode	Electrolyte	Cathode
Material	Ni-YSZ	YSZ	LSM
Density (kg/m^3)	6870	6570	5900
Young's modulus (GPa)	57	215/185	35
Poisson's coefficient	0.28	0.32/0.313	0.36
Tensile yield strength (MPa)	115	332/256	155
Compressive strength (MPa)	100	1000	100
Specific surface area (m^{-1})	1e9	-	1x10^9
Coefficient of thermal expansion (K^{-1})	12.2x10^{-7}	10.3x10^{-7}	11.7x10^{-7}
Permeability (m^2)	1e-12	--	1x10^{-12}
Effective electronic conductivity (S/m)	13195	--	801.01
Effective ionic conductivity (S/m)	0.51364	--	0.51364
Stress intensity factor (MPa*m$^{0.5}$)	1.6	1.79	1.24

Table 2. Geometrical parameters of the SOFC.

Channel width (mm)	60
Channel height (mm)	0.35
Anode thickness (mm)	0.25
Anode width (mm)	60
Cathode thickness (mm)	0.06
Cathode width (mm)	60
Electrolyte thinks (mm)	0.01
Electrolyte width (mm)	60

All properties of fluids fluctuate with temperature and are presumed here to perform as ideal gas, and they are estimated according to the ideal gas mixture law. In addition, steady flow is presumed to be incompressible, two-dimensional, and laminar. Fully impermeable electrolyte and eclectic electrodes in the following reactions take place in the electrodes. Other assumptions are as follows:

- Thermal diffusion is neglected.
- Ohmic heat due to electron transfer is neglected because electronic conductivity in electrodes is higher than ionic conductivity.
- The Darcy equation is used to model mass transport in porous electrodes.
- The convective diffusion term is neglected due to low permeability in porous electrolyte (electrolyte is impermeable).
- Electrolyte is insulated to electron transfer.

The following reactions take place in the electrodes:

Anode reaction:

$$H_2 + O^{-2} \rightarrow H_2O + 2e^- \quad (1)$$

Cathode reaction:

$$\frac{1}{2}O_2 + 2e^- \rightarrow O^{-2} \quad (2)$$

The overall reaction is given by:

$$H_2 + \frac{1}{2}O_2 \rightarrow H_2O \quad (3)$$

2.1. Mass and momentum conservation

The continuity equation in porous electrode is given by [18]:

$$\nabla.(\rho \mathbf{u}) = \sum_j R_j \quad (4)$$

The momentum equation for stationary and incompressible flow in porous electrodes with no body force is expressed by Darcy law as follows [20]:

$$\rho \mathbf{u}.\nabla \mathbf{u} = \nabla.\left(-p\mathbf{I} + \frac{\mu}{\in}\left(\nabla \mathbf{u} + (\nabla \mathbf{u})^T\right) - \frac{2\mu}{3}(\nabla.\mathbf{u})\mathbf{I}\right) + \rho \mathbf{g} - \left(\frac{\mu}{\kappa}\right)\mathbf{u} \quad (5)$$

where u is the flow velocity, K is the permeability, μ is the dynamic viscosity, and P is the absolute pressure. The momentum transport in fuel and air channel is applied by the Navier-Stoeks equation.

$$\rho(\mathbf{u}.\nabla)\mathbf{u} = \nabla.[-p\mathbf{I} + \mu(\nabla \mathbf{u} + (\nabla \mathbf{u})^T] \quad (6)$$

2.2. Species conservation

For an individual species, the species equation is determined by [20]:

$$\nabla.j_i + \rho(u.\nabla)\omega_i = R_i \quad (7)$$

where j_i stands for the diffusive flux of the ith species, and the mass fraction of the ith species is ω_i, R_i is the rate of species' production. The relative mass flux vector is written using the Maxwell-Stefan equations of multi-component systems as follows [17]:

$$j_i = -\rho\omega i \sum_k D_{ik}\, d_k \quad (8)$$

where d_k is the generalized driving force, and D_{ik} is the diffusion coefficient in Fick's law of species (multi-component), which can be determined by [17]:

$$D_{ik} = 1.883\times10^{-2} T^{1.5} \frac{\left(\frac{1}{M_i} + \frac{1}{M_k}\right)^{1/2}}{p\sigma_{ik}^2 \Omega_D} \quad (9)$$

where the diffusion collision integral is Ω_D, the characteristic length is σ, and M is the molecular weight. To study mass transfer resistance in the porous electrodes, the multi-component Fick's diffusivities are revised using the succeeding equation [17]:

$$D_{ik}^{eff} = \left(\frac{\varepsilon}{\tau}\right) D_{ik} \quad (10)$$

where τ is the porous media tortuosity. Dusty Gas Model (DGM) is applied to interpret for Knudsen tiny pores

diffusion. The effective DGM diffusion of coefficient ($D^{eff}_{DGM,ik}$) is defined as follows [17]:

$$D^{eff}_{DGM,ik} = \frac{\left(\frac{\varepsilon}{\tau}\right)\left(D_{ik} \cdot D_{KN,ik}\right)}{\left(D_{ik} + D_{KN,ik}\right)} \quad (11)$$

The Knudsen diffusivities coefficient is $D_{KN,ik}$ and is calculated by the kinetic theory of gases as follows [17]:

$$D^{eff}_{KN,ik} = \frac{4}{3r_e\sqrt{\frac{R_u T(M_i+M_k)}{\pi M_i . M_k}}} \quad (12)$$

Actual pore radius is r_e, and Ru is the ideal gas constant.

2.3. Energy conservation

The energy equation for laminar, steady, incompressible and low speed is given by [22]:

$$\nabla.(\rho C_p \mathbf{u}.T - K\nabla T) = Q \quad (13)$$

where ρ is density, C_p is heat capacity at constant pressure, and Q is the heat source due to ion electronic transport resistance in each of the three layers and is determined by:

$$Q = \frac{j_{io}^2}{\sigma_{io}} \quad (14)$$

J_{io} and σ_{io} are the ionic current density and conductivity, respectively [19].

2.4. Charge conservation

Using Ohm's law, the governing electron conservation and ion transfer equations are, respectively, as follows [23]:

$$\nabla.(-\sigma_e \nabla\varphi_e) = j_e \quad (15)$$

$$\nabla.(-\sigma_i \nabla\varphi_i) = j_i \quad (16)$$

where j_e and j_i are the electronic and ionic sources, σ_e is electronic conductivity, and σ_i is the ionic conductivity.

The electrical charge source (j_e) and ionic charge source (j_i) for each anode and cathode catalyst layer are formulated by the Bulter-Volmer equation, respectively, as follows [24]:

$$j_{i,a} = -j_{e,a} = A_a j^{H_2}_{0.ref}\left(\frac{C_{H_2}}{C_{H_{2.ref}}}\right)^{\gamma H_2}\left[\exp\left(\frac{\alpha^a_a F \eta_{act,a}}{R_u T}\right) - \exp\left(-\frac{\alpha^a_c F \eta_{act,a}}{R_u T}\right)\right] \quad (17)$$

$$j_{e,c} = -j_{i,c} = A_c j^{O_2}_{0.ref}\left(\frac{C_{O_2}}{C_{O_{2.ref}}}\right)^{\gamma O_2}\left[\exp\left(\frac{\alpha^c_a F \eta_{act,c}}{R_u T}\right) - \exp\left(-\frac{\alpha^c_c F \eta_{act,c}}{R_u T}\right)\right] \quad (18)$$

where A is the electrochemically active surface area per unit volume, and $j^{H_2}_{0.ref}$ and $j^{O_2}_{0.ref}$ are reference exchange current densities. The reaction order for hydrogen oxidation at hydrogen reference concentration ($C_{H_{2.ref}}$) is γH_2, and reaction order for oxygen reduction at oxygen reference concentration ($C_{O_{2.ref}}$) is γO_2. The charge transfer coefficient is α and its value is between 0 and 1, F is Faraday's constant equal to 96,487 C/mol, and η_{act} is the activation overpotential. The subtitles "a" and "c" stand for anode and cathode sides. The anode activation overpotential (η_a) and the cathode activation overpotential (η_c) are determined, respectively, as follows:

$$\eta_a = \varphi_e - \varphi_i. \quad (19)$$

$$\eta_c = \varphi_e - \varphi_i - V_{oc} \quad (20)$$

anywhere φ_e is the electronic potential, and φ_i is the ionic potential. V_{oc} is the open-circuit voltage calculated by the Nernst's equation [5]:

$$V_{OC} = 1.317 - 2.769\times10^{-4}T + R_u T/2F \ln\left(p_{H_2}.p^{1/2}_{O_2}/p_{H_2O}.p^{1/2}_{ref}\right) \quad (21)$$

where P_{ref} is the total pressure, and F is Faraday's constant.

2.5. Thermal stress

In this study, the detection of crack initiation is done by thermal stress. First, the thermal strain, $\alpha(T - T_{ref})$, is calculated and, then, thermal stress, σ_{ii}, is determined by the strain, ε_{ii}, as defined by [25]:

$$\varepsilon_{xx} = \frac{1}{E}(\sigma_{xx} - \nu\sigma_{yy}) + \alpha(T - T_{ref}) \quad (22)$$

$$\varepsilon_{yy} = \frac{1}{E}(\sigma_{yy} - \nu\sigma_{xx}) + \alpha(T - T_{ref}) \quad (23)$$

$$\varepsilon_{xy} = \frac{1}{2G}\sigma_{xy} \quad (24)$$

where $\frac{1}{E}(\sigma_{xx} - \nu\sigma_{yy})$ is the mechanical strain, α is the coefficient of thermal expansion, T is the temperature, T_{ref} is the strain reference temperature, E is Young's ratio, and nu is the Poisson's ratio. The shear modulus, G, is defined as follows:

$$G = \frac{E}{2(1+nu)} \quad (25)$$

By rearranging Eqs. (22) and (23), the stress in x and y directions is determined, respectively, as follows:

$$\sigma_{xx} = 2G\left[\varepsilon_{xx} + \frac{nu}{1-2nu}\left(-\frac{1+nu}{nu}\alpha(T - T_{ref})\right)\right] \quad (26)$$

$$\sigma_{yy} = 2G\left[\varepsilon_{yy} + \frac{nu}{1-2nu}\left(-\frac{1+nu}{nu}\alpha(T - T_{ref})\right)\right] \quad (27)$$

$$\sigma_{xy} = 2G\varepsilon_{xy} \quad (28)$$

2.6. Strain-displacement equation

Strain displacement equations, also called kinematic equations or Infinitesimal deformations, are as follows [26]:

$$\varepsilon_{xx} = \frac{\partial u}{\partial x} \quad (29)$$

$$\varepsilon_{yy} = \frac{\partial v}{\partial y} \quad (30)$$

$$2\varepsilon_{xy} = \frac{\partial u}{\partial x} + \frac{\partial v}{\partial x} \quad (31)$$

where u and v are the displacements, which represent the unit charge in length of a line element.

2.7. Conservation of momentum for solid mechanics

The equation of motion is given by [26]:

$$\sigma_{ij,j} + X_i = \rho\ddot{u}_i \quad (32)$$

Considering that the body force, X_i, and the acceleration of the particles inside the material, $\ddot{u}_i$, are zero, the equation of motion, Eq. (26), reduces to:

$$\sigma_{ij,j} = 0 \tag{33}$$

Or

$$\frac{\partial \sigma_{xx}}{\partial x} + \frac{\partial \sigma_{xy}}{\partial y} = 0 \tag{34}$$

$$\frac{\partial \sigma_{yx}}{\partial x} + \frac{\partial \sigma_{yy}}{\partial y} = 0 \tag{35}$$

And

$$\sigma_{xy} = \sigma_{yx} \tag{36}$$

2.8. Navier equation

Navier, also called displacement, equations of thermos-elasticity in x and y directions are respectively expressed as follows [25]:

$$(\lambda + \mu)\frac{\partial e}{\partial x} + \mu \nabla^2 u - (3\lambda + 2\mu)\alpha \frac{\partial T}{\partial x} + X = 0 \tag{37}$$

$$(\lambda + \mu)\frac{\partial e}{\partial y} + \mu \nabla^2 v - (3\lambda + 2\mu)\alpha \frac{\partial T}{\partial y} + Y = 0 \tag{38}$$

where e is given by:

$$e = \frac{\partial u}{\partial x} + \frac{\partial v}{\partial y} \tag{39}$$

where X and Y are the x-axis and y-axis body forces, respectively, and they are equal to zero. λ and μ are the Lame elastic constants and are respectively defined as follows:

$$\lambda = \frac{nu\ E}{(1 + nu)(1 - 2\,nu)} \tag{40}$$

$$\mu = G = \frac{E}{2(1 + nu)} \tag{41}$$

Substituting Eqs. (40) and (41) into Eqs. (37) and (38) respectively gives the displacement equations in terms of Young's module as follows [25]:

$$\frac{E}{2(1-v)}\frac{\partial}{\partial x}\left(\frac{\partial u}{\partial x} + \frac{\partial v}{\partial y}\right) + \frac{E}{2(1+v)}\nabla^2 u - \frac{\alpha E}{1-v}\frac{\partial T}{\partial x} = 0 \tag{42}$$

$$\frac{E}{2(1-v)}\frac{\partial}{\partial y}\left(\frac{\partial u}{\partial x} + \frac{\partial v}{\partial y}\right) + \frac{E}{2(1+v)}\nabla^2 v - \frac{\alpha E}{1-v}\frac{\partial T}{\partial y} = 0 \tag{43}$$

where ∇^2 is the Laplacian operator.

2.9. Energy equation

The energy equation for the porous electrodes is [26]:

$$K\nabla^2 T + \frac{Q}{K} + (3\lambda + 2\mu)T_0\dot{\varepsilon} = \frac{1}{\alpha}\frac{\partial T}{\partial t} \tag{44}$$

where the coupling term between temperature and stress is $\dot{\varepsilon}$, α is the linear thermal expansion coefficient, and T_0 is the reference temperature.

2.10. Stress intensity factor

The crack initiation is according to the built-up stress caused by temperature and the physical mismatch of the cell layer's properties. When the stiffness value of the cell layer is higher than the stress intensity factor or is equal to the critical fracture toughness, the mismatch between cell layers appears, which will lead to crack initiation. The stress intensity factor, K_I, is calculated by using the so-called J-integral. The J-integral formula is represented as follows [26]:

$$J = \int_\Gamma W dy - T_i \frac{\partial u_i}{\partial x} ds = \int_\Gamma (W n_x - T_i \frac{\partial u_i}{\partial x}) ds \tag{45}$$

where W is the strain energy density

$$W = \frac{1}{2}(\sigma_x . \varepsilon_x + \sigma_y . \varepsilon_y + \sigma_{x.y} . 2 . \varepsilon_{xy}) \tag{46}$$

and T is the traction vector defined as follows:

$$T = [\sigma_x . n_x + \sigma_{xy} + \sigma_{xy} . n_x + \sigma_y . n_y] \tag{47}$$

σ_{ij} denotes the stress components, ε_{ij} is the strain components, and n_i is the normal vector components. The relation between stress intensity factor and J-integral is represented as:

$$J = \frac{K_I^2}{E} \tag{48}$$

where Young's modulus is represented by *E*.

3. BOUNDARY CONDITION

To model crack initiation, the following expectations are utilized:

- Thermal diffusion is neglected.
- Stokes–Brinkman's assumption is neglected.
- Ohmic heat due to electron transfer is neglected because electronic conductivity in anode electrode is higher than ionic conductivity.
- All gasses behave as ideal gases.
- Darcy's equation models the mass transport in anode and cathode porous electrodes.
- Coupling effect between the thermal and mechanical equations is neglected.

Based on the model provided in Figure 1, the following boundary conditions are applied.

3.1. Inlet assumption

V=0 At the anode electrode boundary.

U=U_{in}

T=T_0

w_i = specified (mass fraction of the species).

No-slip boundary condition is valid in all electrolyte boundaries due to U=0.

3.2. Outlet assumption

a) The conduction term compared to the convection term can be neglected.
b) Convection term is assumed to be the dominant term concerning the mass transport model.

4. NUMERICAL PROCEDURE

A computational fluid dynamic (CFD) code based on a finite element method was developed and utilized. The code used a mapped rectangular mesh, which consists of 725000 elements, 1285257 degrees of freedom. The distribution of mesh numbers increases at the electrolyte–anode and electrolyte–cathode zones, where the high tempture and high pressure are

likely to occur. The mesh numbers decreased as it moving away from the electrolyte to the gas channel. The fuel is hydrogen, and the SOFC operates at 0.8V continuous voltage. The code obtains the temperature and stress distribution in the following manner:

1) The code initially solves the secondary current distribution equation, Eq. (15-21).
2) Then, the code solves the non-linear momentum equations, Eqs. (5) and (6), for anode and cathode, respectively.
3) Furthermore, the code solves the species and the Stefan–Maxwell equations, Eqs. (7) to (12), for anode and cathode.
4) Finally, the code solves the energy equation for porous cathode and anode and for solid electrolyte, Eqs. (13) and (14).

The obtained temperature distribution is used to solve the strain equations, Eqs. (22)-(28), to determine the thermal stress distribution. Then, the code solves the strain displacement equations, Eqs. (29)-(43), and locates the initiation of the crack using the stress intensity factor and J Integral equations, Eqs. (44)-(48).

5. RESULTS AND DISCUSSION

In order to confirm the results, the current model is modified and compared to Roger's experimental data [27]. Figure 2 reveals the comparison between the experimental and current studies. Input parameters of the current study were extracted from the studies of Hussain [28], Ghassemi [9], and Shao [29, 30] (The rest of the validation input parameters are shown in Table 3). This comparison shown in Fig. 2 reveals coherent results between the current study and that of Rogers with a mean square error of about 1 %.

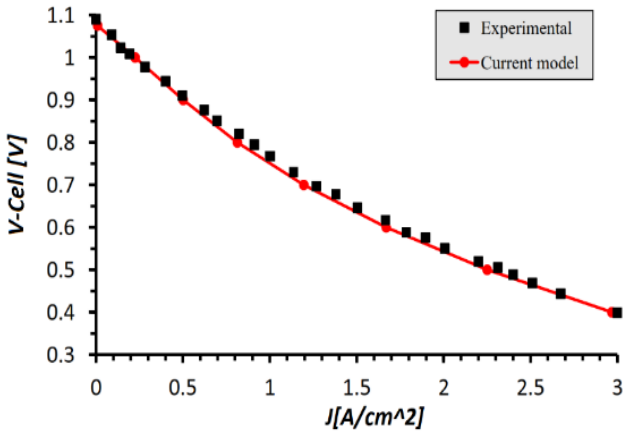

Figure 2. The current model's accuracy compared to experimental data provided by Rogers.

Figures 3 and 4 depict the pressure distribution in anode and cathode electrodes, respectively. The maximum pressure at the anode porous electrode is at the fuel inlet. The pressure at the contact between anode electrode and anode gas channel is about 12 Pa and decreases as it gets closer to electrolyte. However, the maximum pressure at the cathode reaches about 17 Pa at the inlet and decreases to 5 Pa in the middle of cathode electrode and, then, to zero as we move to the outlet. This phenomenon results from the chemical reaction that in this zone begins to react more than in other zones.

Table 3. Validation input parameter.

Description	Symbol	Value	Unit
Operating temperature	T	800	^{o}C
Pressure	P_0	101335	P_a
Conductivity of electrolyte	σ	0.64	S/m
Conductivity of anode	σ	71428.57	S/m
Conductivity of cathode	σ	5376.34	S/m
Inlet velocity of fuel channel	$V_{in\ (fuel)}$	0.4	m/s
Inlet velocity of air channel	$V_{in\ (air)}$	0.8	m/s
Porosity of porous electrodes	ε	0.375	-
Tortuosity of porous electrodes	τ	4.5	-
Thermal conductivity of anode	k_a	6.23	W/m.K
Thermal conductivity of cathode	k_c	10	W/m.K
Thermal conductivity of electrolyte	k_e	2.7	W/m.K
Specific heat of anode	$C_{p,a}$	595	J/Kg.K
Specific heat of cathode	$C_{p,c}$	573	J/Kg.K
Specific heat of electrolyte	$C_{p,e}$	606	J/Kg.K

Anode electrode

Left side (out let, x= 0.3)

Middle (x=30)

Right side (out let, x= 59)

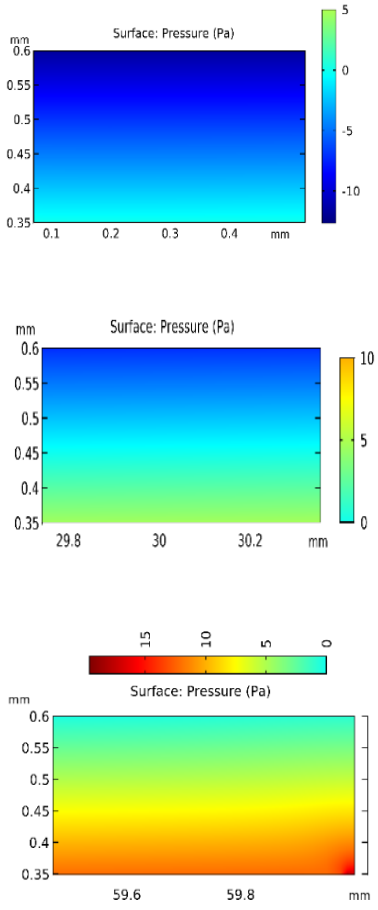

Figure 3. Pressure distribution at anode electrode.

Cathode electrode

Left side (out let, x= 0.3)

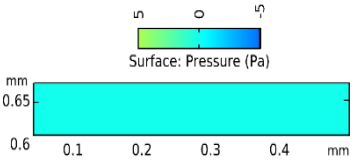

Middle (x=30)

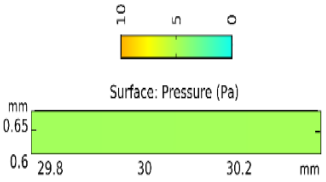

Right side (out let, x= 59)

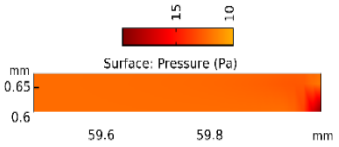

Figure 4. Pressure distribution at cathode electrode.

Figures 5 to 7 depict the temperature distribution in the anode, cathode, and the entire fuel cell, respectively. As shown in the figures, the temperature varies from 500 ^{o}C to 1100 ^{o}C. The maximum temperature is in the middle of the channel near the anode electrode and decreases as moving away from it.

Figures 5,6 depict the temperature allocation at anode and cathode electrodes, respectively. Again, the maximum temperature is in the middle of the electrodes and decreases as moving away from it.

Anode electrode

Left side (out let, x= 0.3)

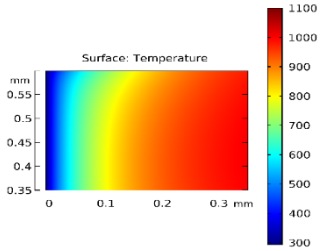

Middle (x=34)

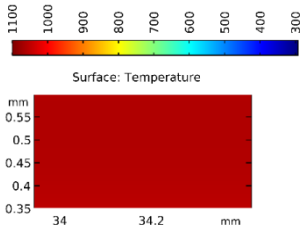

Right side (outlet, x= 59)

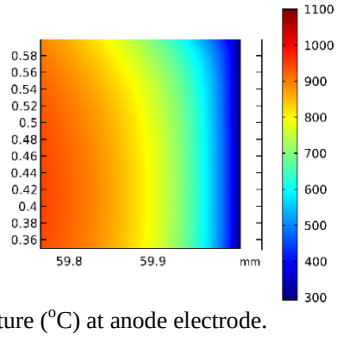

Figure 5. Temperature (^{o}C) at anode electrode.

Cathode electrode

Left side (out let, x= 0.3)

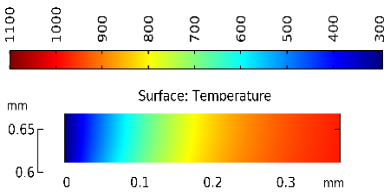

Middle (x=34)

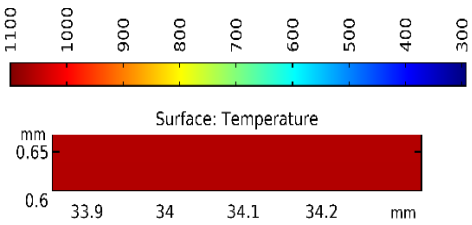

Right side (out let, x=59)

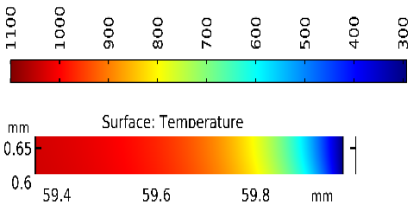

Figure 6. Temperature (^{o}C) at cathode electrode.

Figure 7 depicts the temperature distribution at the entire SOFC. As shown, the following results are observed:

- The temperature distribution is affected by reforming and electrochemical reactions.
- In the anode gas channel, the temperature varies from 500 ^{o}C to 1100 ^{o}C. The maximum temperature is in the middle of the fuel channel near the anode electrode and decreases as moving away from it.
- In anode electrode, the maximum temperature is in the middle and decreases as moving away from it.
- There is a heat balance between endothermic and exothermic electrochemical reactions, and a higher temperature appears in the active layer near electrolyte.
- It can be seen that temperature increases rapidly between the air inlet located at the upper right corner and the air outlet located at the lower left corner due to the exothermic electrochemical reactions.
- It is shown that the evolution of heat generated by the electrochemical reactions tends to diffuse by the conduction and convection towards the gas flow channels.
- When the temperature increases, it enhances the rate of electrochemical reaction at the reaction sites and increases the electronic and ionic conductivities of the electron and ion-conducting particles, respectively. This in turn minimizes the Ohmic contribution to the total cell potential loss and, thereby, enhances the cell performance. Accordingly, under typical SOFC operating conditions, the temperature increase leads to a decrease in the activation overpotential, since the exchange current density is an increasing function of temperature.
- In the porous electrodes, the formed gradients of H_2 and O_2 molar concentrations are larger than those in the fuel and air channel, because the diffusion is more difficult in the porous electrodes than that in the fuel and air

channels. Additionally, at the fuel and air channels, the convective effects are much larger than the porous electrodes, where diffusion prevails. Finally, at higher temperatures, the diffusivity of the species is increased, resulting in lower values of concentration overpotentials, as the species can diffuse easier through the porous diffusion layer. Higher operating temperatures result in not only lower reversible voltages, as expected by Eq. (15), but also higher limiting current density values.

Entire SOFC

Left side (out let, x= 0.3)

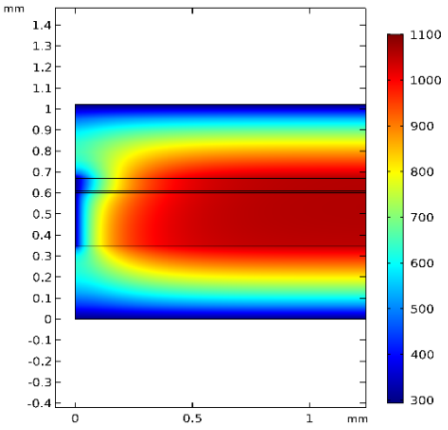

Left side (out let, x= 34)

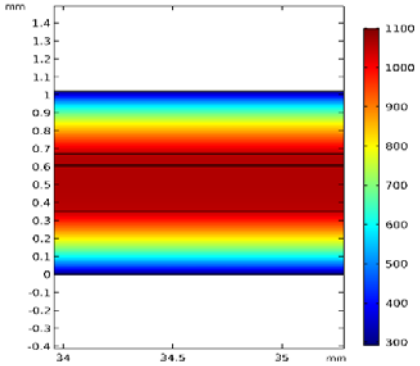

Right side (out let, x= 59)

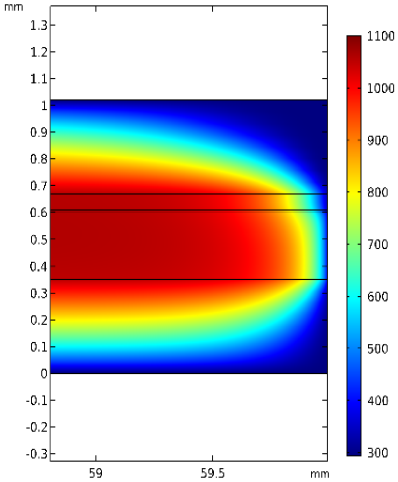

Figure 7. Temperature (^{o}C) at the entire SOFC.

Figure 8 depicts the anode thermal stress distribution. As shown, the highest thermal stress occurs at the right and left corners of the bottom wall, where it is in contact with fuel channel. Since the highest temperature distribution takes place at this location and temperature is expected to exceed the threshold value dictated by the SOFC anode materials, the mechanical failure of the anode takes place.

Anode electrode

Left lower part

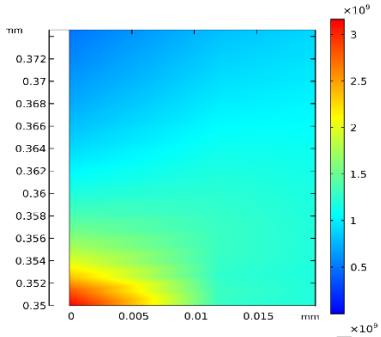

Right lower part

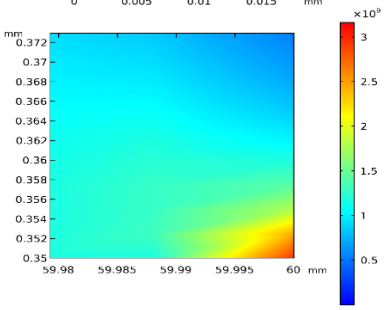

Figure 8. Anode thermal stress (Pa).

Figure 9 shows the cathode electrode thermal stress distribution. As is shown, the highest thermal stress is at the right and left corners of the upper wall, where it is in contact with air channel. Again, since the highest temperature distribution takes place at this location and temperature is expected to invade the threshold values transcribed by the SOFC cathode materials, the mechanical failure of the cell takes place.

Cathode electrode

Left upper part

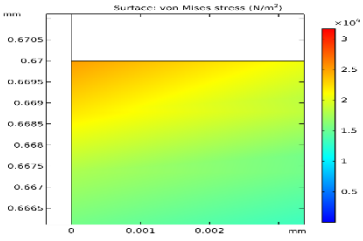

Right upper part

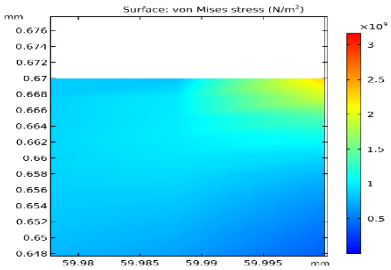

Figure 9. Cathode thermal stress (Pa).

Figures 10 and 11 depict the displacement distribution in the anode and cathode electrodes. From these 2 figures, it is shown clearly that there is a high displacement in the cathode electrodes. The maximum displacement is found to be between the lower and upper corners of the cathode. Based on the previous result regarding the location of the maximum thermal stress and the maximum pressure, it is logical to have the weakest points at the cathode inlet and outlet walls.

Therefore, the location of the displacement in the middle of the lower and upper corners of the cathode is logical, too. In other words, it is expected for the crack to initiate at this location.

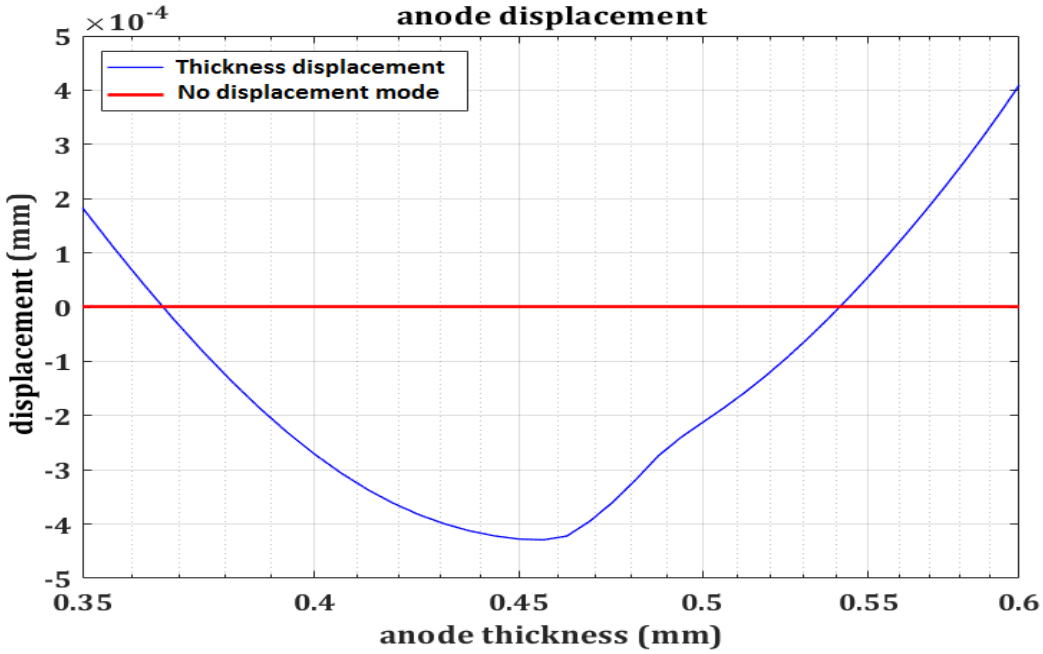

Figure 10. Anode displacement.

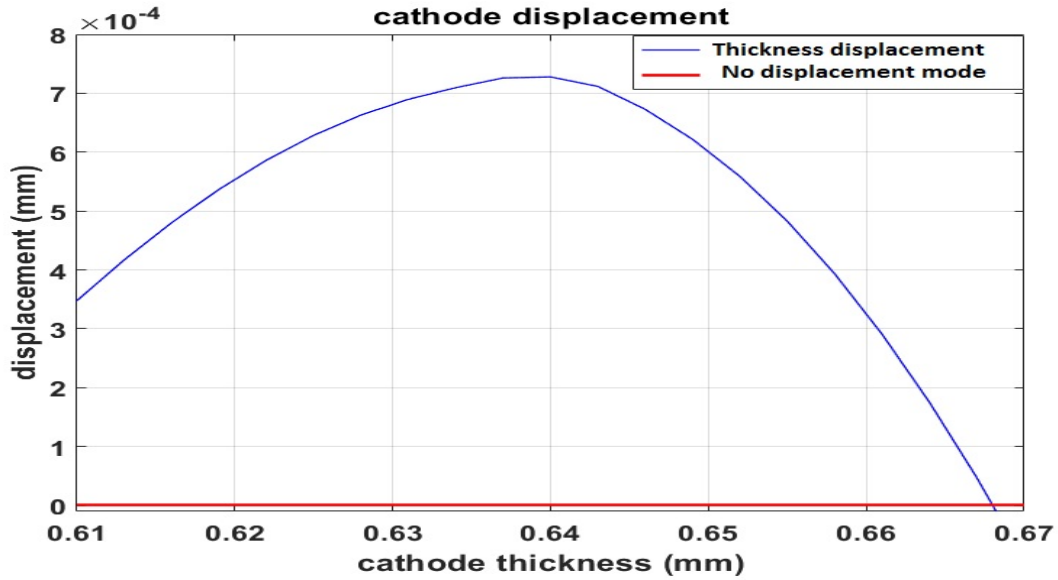

Figure11. Cathode displacement.

6. CONCLUSIONS

The current study presents the result of the prediction of crack in SOFC. The fuel is hydrogen, operating temperature is between 800 ^{o}C to 1000 ^{o}C, and the SOFC operates at 0.8V continuous voltage. The following results are obtained:

- The temperature distribution was concentrated in the middle of the contact area between cathode and electrolyte up to the center of the cathode electrode.
- The pressure at the contact between anode electrode and anode gas channel is about 12 atm and decreases as it gets closer to electrolyte. However, the maximum pressure at the cathode reaches about 17 atm at the inlet and decreases to 5 atm in the middle of the cathode electrode and, then, to zero as we move to outlet.
- The stress distribution was detected at the upper corners of the cathode with much more stress at the left corner than the right corner.
- The displacement distribution in cathode is maximum at both inlet and outlet from the lower corner to the upper corner.
- The stress intensity factor in cathode is lower than that in anode.
- This expectation is based on the temperature, pressure, and thermal stress.

The life ime of the cell with crack decreases by 40 to 50 %. Therefore, the expected lifetime is about 2500 hr to 3000 hr.

7. ACKNOWLEDGEMENT

This work is supported by Nano and Fuel cell lab in K.N. Toosi university and JIA Engineering lab Beirut Lebanon, The authors thankfully and gratefully for supporting this study.

REFERENCES

1. Hoogers, G., Fuel cell technology handbook, CRC Press, Boca Raton, (2003), 200-230.
2. Hibino, T., Hashimoto, A., Yano, M., Yoshida, S.I. and Sano, M., "High performance anodes for SOFCs operating in methane-air mixture at reduced temperatures", ***Journal of Electrochemistry Society***, Vol. 149, (2002), 133-136. (Doi: 10.1149/1.1430226).
3. Zhu, H., Kee, R.J., Janardhanan, V.M., Deutschmann, O. and Goodwin, D.G.,"Modeling elementary heterogeneous chemistry and electrochemistry in solid-oxide fuel cells", ***Journal of Electrochemistry Society***, Vol. 152, (2005), 2427-2440. (Doi: 10.1149/1.2116607).
4. Greco, F., Frandsen, H.L., Nakajo, A., Madsen, M.F. and Van herle, J., "Modelling the impact of creep on the probability of failure of a solid oxide fuel cell stack", ***Journal of The European Ceramic Society***, Vol. 34, (2014), 2695-2704. (Doi: 10.1016/j.jeurceramsoc.2013.12.055).
5. M. Peksen, "Numerical thermomechanical modelling of solid oxide fuel cells", ***Progress in Energy and Combustion Science***, Vol. 48, (2015), 1-20. (Doi: 210.1002/9783527650248.ch27).
6. Boccaccini, D.N., Sevecek, O., Frandsen, H.L., Dlouhy, I., Molin, S., Cannio, M., Hjelm, J. and Hendriksen P.V, "Investigation of the bonding strength and bonding mechanisms of SOFCs interconnector-electrode interfaces", ***Material Letters***, Vol. 162, (2016), 250-253. (Doi:1 0.1016/j.matlet.2015.07.137).
7. Xu, M., Li, T., Yang, M. and Anderson, M., "Solid oxide fuel cell interconnect design optimization considering the thermal stresses", ***Science Bulletin***, Vol. 61, No. 17, (2016), 1333-1344. (Doi: 10.1007/s11434-016-1146-3).
8. Fleischhauer, F., Terner, M., Bermejo, R., Danzer, R., Mai, A., Graule, T. and Kuebler, J., "Fracture toughness and strength distribution at room temperature of zirconia tapes used for electrolyte supported solid oxide fuel cells", ***Journal of Power Sources***, Vol. 275, (2015), 217-226. (Doi: 10.1016/j.jpowsour.2014.10.083).
9. Kamvar, M., Ghasemi, M. and Rezaei, M., "Effect of catalyst layer configuration on single chamber solid oxide fuel cell performance", ***Applied Thermal Engineering***, Vol. 100, (2016), 98-104. (Doi: 10.1016/j.applthermaleng.2016.01.128).
10. Pianko-Oprych, P., Zinko, T. and Jaworski, Z., "A numerical investigation of the thermal stresses of a planar solid oxide fuel cell", ***Materials***, Vol. 9,No. 10, (2016), 814-831. (Doi: 10.3390/ma9100814).
11. Celik, S., Ibrahimoglu, B., DMat, M., Kaplan, Y. and Veziroglu, T.N, "Micro level two dimensional stress and thermal analysis anode/electrolyte interface of a solid oxide fuel cell", ***International Journal of Hydrogen Energy***, Vol. 40, No. 24, (2015), 7895-7902. (Doi: 10.1016/j.ijhydene.2014.10.057).
12. Luo, Y., Jiang, W., Zhang, Q., Zhang, W.Y. and Hao, M., "Effects of anode porosity on thermal stress and failure probability of planar solid oxide fuel cell with bonded compliant seal", ***International Journal of Hydrogen Energy***, Vol. 41, No. 18, (2016), 7464-7474. (Doi:10.1016/j.ijhydene.2016.03.117).
13. Kong, W., Zhang, W., Zhang, S., Zhang, Q. and Su, S., "Residual stress analysis of a micro-tubular solid oxide fuel cell", ***International Journal of Hydrogen Energy***, Vol. 41, No. 36, (2016), 16173-16180, (Doi: 10.1016/j.ijhydene.2016.05.256).
14. Fan, P., Li, G., Zeng, Y. and Zhang, X., "Numerical study on thermal stresses of a planar solid oxide fuel cell", ***International Journal of Thermal Sciences***, Vol. 77, (2014), 1-10. (Doi: 10.1115/ FUELCELL2017-3176).
15. Pianko-Oprych, P., Zinko, T. and Jaworski, Z., "Modeling of thermal stress in amicrotubular solid oxide fuel cell stack", ***Journal of Power Sources***, Vol. 300, (2015), 10-23. (Doi: doi.org/10.1016/j.jpowsour. 2015.09.047).
16. Pianko-Oprych, P., Zinko, T. and Jaworski, Z., "A numerical investigation of the thermal stresses of a planar solid oxide fuel cell", ***Materials (Basel)***, Vol. 9, No. 10, (2016). (Doi: 10.3390/ma9100814).
17. Ho, T.X., Kosinski, P., Hoffmann, A.C. and Vik, A.,"Effects of heat sources on the performance of a planar solid oxide fuel cell", ***International Journal of Hydrogen Energy***, Vol. 35, No. 9, (2010), 4276-4284. (Doi: 10.1016/j.ijhydene.2010.02.016).
18. Bove, R. and Ubertini, S., Modeling solid oxide fuel cells methods, procedures and techniques, Fuel cell and hydrogen energy, Springer, New York, United States, (2008). (Doi: 10.1007/978-1-4020-6995-6).
19. Larminie, J. and Dicks, A., Fuel cell systems explained, Second edition, John Wiley, New York, (2003). (Doi: 10.1002/9781118878330).
20. Singh, P. and Bansal, P., Advances in solid oxide fuel cells IV, John Wiley, New York, (2008). (Doi: 10.1002/9780470456309).
21. Taylor, R. and Krishna, R., Multicomponent mass transfer, First edition, John Willey, (1993).
22. Nehter, P., Theoretical analysis of high fuel utilization solid oxide fuel cell, Nova Science Publications, New York, (2008).
23. Akhtar, N., Decent, S.P., Loghin, D. and Kendall, K., "A three dimensional numerical model of a single-chamber solid oxide fuel cell", **I*nternational Journal. Hydrogen Energy***, Vol. 34, No. 20, (2009), 8645-8663. (Doi: 10.1016/j.ijhydene.2009.07.113).
24. Milewski, J., Świrski, K., Santarelli, M. and Leone, P., Advanced methods of solid oxide fuel cell modeling, Springer Publication, New York, USA, (2011). (Doi: 10.1007/978-0-85729-262-9).
25. Boley, B.A. and Weiner, J.H., Theory of thermal stresses, Dover Publication, New York, (1997).
26. Hetnarski, R.B. and Eslami, M.R., Thermal stress: Advanced in theory, Springer Publication, New York, (2008). (Doi: 10.1007/978-1-4020-9247-3).
27. Rogers, W.A., Gemmen, R.S., Johnson, C., Prinkey, M. and Shahnam, M., "Validation and application of a CFD-based model for solid oxide fuel cells and stacks", ***Proceedings of ASME 2003 1st International Conference on Fuel Cell Science, Engineering and Technology***, (2003), 517-520. (Doi: 10.1115/FUELCELL2003-1762).
28. Hussain, M.M., Li, X. and Dincer, I., "Mathematical modeling of planar solid oxide fuel cells", ***Journal of Power Sources***, Vol. 161, No. 2, (2006), 1012-1022. (Doi: 10.1016/j.jpowsour.2006.05.055).
29. Shao, Q., Bouhala, L., Fiorelli, D., Fahs, M., Younes, A., Núñez, P., Belouettar, S. and Makradi, A., "Influence of fluid flow and heat transfer on crack propagation in SOFC multi-layered like material with anisotropic porous layers", ***International Journal of Solids and Structures***, Vol. 97, (2016), 189-198. (Doi: 10.1016/j.ijsolstr. 2015.08.026).
30. Shao, Q., Fernández-González, R., Ruiz-Morales, J.C., Bouhala, L., Fiorelli, D., Younes, A., Núñez, P., Belouettar, S. and Makradi, A., "An advanced numerical model for energy conversion and crack growth predictions in solid oxide fuel cell units", ***International Journal of Hydrogen Energy***, Vol. 40, No. 46, (2015), 16509-16520. (Doi: 10.1016/j.ijhydene.2015.10.016).